TECHNICAL ARTICLE

Resistance of Quench and Partitioned Steels Against Hydrogen Embrittlement

Hamdi Elsayed, Andreas Drexler, Fernando Warchomicka, Ines Traxler, Josef Domitner, Matthew Galler, Rudolf Vallant, and Christof Sommitsch

Multiphase ultra-high strength steels (UHSS) containing retained austenite (RA) appear to be among the most interesting steels for the automotive industry. Developments in the last decades have allowed obtaining a very good combination of mechanical strength and ductility. Quenching and partitioning (Q&P) steels have been proposed as third-generation UHSS, reaching ultimate tensile strength up to 1300 MPa along with excellent fracture elongations of more than 15%. However, the use of Q&P steels is mainly limited by their susceptibility to hydrogen embrittlement (HE). The present work investigates the influence of the Q&P heat treatment parameters on the mechanical properties and on the HE resistivity of 20Mn-Si wire rod steel. The HE resistivity was measured using incremental step load testing with in situ electrochemical hydrogen charging according to ASTM F1624-12 standard. A comprehensive microstructure characterization was performed to examine volume fraction, nucleation sites and morphologies of RA. Although the mechanical properties were similar after Q&P heat treatment, an increase in the partitioning time revealed a significant increase in the HE threshold stress of more than 200 MPa.

Keywords	hydrogen, hydrogen embrittlement (HE), incremental step load test (ISLT), quenching and partitioning (Q&P), ultra-high strength steels (UHSS)

Abbreviations

ASTM	American Society for Testing and Materials
bcc	Body-centered cubic
bct	Body-centered tetragonal
b RA	Blocky retained austenite
DP	Dual-phase
DIN	Deutsches Institut für Normung
EBSD	Electron backscatter diffraction
EDX	Energy-dispersive x-ray spectroscopy
fcc	Face-centered cubic
f RA	Filmy retained austenite
HE	Hydrogen embrittlement
HV	Vickers hardness [HV10]
ISLT	Incremental step load test
KM	Koistinen–Marburger
LOM	Light optical microscopy
Q&P	Quenching and partitioning
Q&T	Quenching and tempering
RA	Retained austenite
TDA	Thermal desorption analysis
TRIP	Transformation-induced plasticity
SEM	Scanning electron microscopy
SSRT	Slow strain rate testing
TEM	Transmission electron microscopy
UHSS	Ultra-high strength steels
XRD	X-ray diffraction

1. Introduction

The automotive industry seeks new technological solutions to increase ultra-high strength steel (UHSS) formability, achieve downsizing by enabling lightweight steel construction, and reduce environmental impacts (Ref 1). Recently developed quenching and partitioning (Q&P) low carbon Mn-Si steels contain martensite and significant volume fractions of retained austenite (RA) (Ref 2, 3). Q&P steels demonstrate excellent mechanical properties, such as high strength combined with high ductility. While the strength is based on the martensitic matrix, including carbides, the ductility is gained by multiple deformation mechanisms in the microstructure, such as dislocation slip in martensite and austenite, as well as by volume expansion and lattice distortion associated with the transformation-induced plasticity (TRIP) effect in austenite. Hence, plastic deformation increases the dislocation density in untransformed austenite by slip and activates the TRIP effect, which is

List of Symbols

A_{c1}	Austenite start temperature [°C]
A_{c3}	Austenite finish temperature [°C]
A_1	Fracture elongation [%]
A_0	Initial cross section [mm^2]
α'	Tempered martensite phase
α_B	Bainitic ferrite phase

Hamdi Elsayed, Andreas Drexler, Fernando Warchomicka, Josef Domitner, Rudolf Vallant, and **Christof Sommitsch**, Institute of Materials Science, Joining and Forming, Graz University of Technology (TUG), Kopernikusgasse 24/I, 8010 Graz, Austria; **Ines Traxler**, Centre for Electrochemistry and Surface Technology (CEST), Viktor-Kaplan Straße 2, 2700 Wiener Neustadt, Austria; and **Matthew Galler**, Voestalpine Wire Rod Austria GmbH, Drahtstraße 1, 8792 St., Peter-Freienstein, Austria. Contact e-mail: hamdi.ahmed@tugraz.at.

c_H	Hydrogen content [wppm]	
β	Fitting coefficient [K^{-1}]	
E	Young's modulus [MPa]	
E_b	Binding energy [kJ/mol]	
$EI_{-1.1V}$	Susceptibility embrittlement index at -1.1 V [%]	
$\bar{\bar{\varepsilon}}$	Average strain rate [s^{-1}]	
ε	Engineering strain [%]	
ε	Epsilon carbide	
f_{RA}	Retained austenite volume fraction [vol.%]	
γ	Austenite phase	
j_B	Bodyflux [wppm/s]	
M_s	Martensite start temperature [°C]	
M_f	Martensite finish temperature [°C]	
P	Probability of trapped hydrogen release [-]	
P_F	Fracture force [N]	
P_{th}	Threshold force [N]	
R	Universal gas constant [kJ/Kmol]	
R_m	Ultimate tensile strength [MPa]	
T	Temperature [°C]	
t	Time [s]	
T_Q	Quenching temperature [°C]	
t_Q	Quenching time [s]	
T_P	Partitioning temperature [°C]	
t_P	Partitioning time [s]	
σ	Engineering stress [MPa]	
σ_H	Fracture stress [MPa] in hydrogen donating environment	
σ_{th}	Threshold stress [MPa	

based on the transformation of metastable austenite to untempered martensite. Both deformation mechanisms contribute to the enhanced strain hardening rate of Q&P steels and make them suitable for crash-relevant body-in-white components (Ref 4). However, the TRIP effect in Q&P steels is crucial concerning hydrogen embrittlement (HE). Freshly transformed hard martensite has a negative effect on structural integrity (Ref 5, 6) and can be very susceptible to HE. Hydrogen ingress of a few wppm (Ref 7) during processing or service (e.g., by corrosion or cathodic protection) could already be critical and may cause time-delayed fracture (Ref 8, 9). This concern limits the development and applying new Q&P steels with even higher strength.

Many mechanisms were postulated to explain the deterioration effect of hydrogen on mechanical properties (Ref 10, 11). However, the most relevant mechanisms concerning UHSS are hydrogen-enhanced localized plasticity (HELP), hydrogen-enhanced decohesion (HEDE), adsorption-induced dislocation emission (AIDE) and hydrogen-enhanced strain-induced vacancies (HESIV) (Ref 12, 13). Furthermore, the hydrogen and strain-induced phase transformation mechanism contributes to the understanding of Q&P steels degradation (Ref 14). A combination of mechanisms is involved in many cases depending on the microstructure complexity, macroscopic and microscopic stress and strain state, and the local hydrogen concentration (Ref 15-17). Recently, a simultaneous action of HELP and HEDE has been widely investigated and applied to explain the interaction of hydrogen with the steel microstructure depending on the SEM analysis of the fracture surface (Ref 18-23).

The stability of RA in the martensitic microstructure of Q&P steels and its role in the HE mechanism are controversially discussed. Depending on the actual microstructure characteristics, including carbon or manganese contents, morphology, volume fraction, nucleation sites, and deformation conditions, RA can either be beneficial (Ref 24-27) or detrimental (Ref 5, 6) with respect to HE. Following Pressouyre's theory of deep trapping sites (Ref 28), finely and homogenously dispersed austenite particles may be beneficial for increasing the HE resistivity (Ref 29-31), as long as they are not potential crack nuclei (Ref 5, 6). According to Zhu et al. (Ref 6), the hydrogen concentration in RA particles can reach up to three times the bulk concentration due to the high solubility of hydrogen in the face-centered cubic (fcc) phase (Ref 38, 39). Basically, deep trapping sites have binding energies E_b of more than 60 kJ/mol, causing a negligible probability $P \sim \exp(-E_b/RT)$ of releasing trapped hydrogen at room temperature, with R being the universal gas constant. P also depends on the temperature T, which is crucial with respect to thermally activated hydrogen release and to the deformation characteristics. Thermal activation of trapped hydrogen is usually applied by the so-called thermal desorption analysis (TDA) method to analyze the diffusible hydrogen contents (Ref 32, 33) and to determine corresponding trapping energies (Ref 29, 30, 34, 35). Although some studies revealed deep hydrogen trapping sites related to RA particles after high-temperature gaseous charging (Ref 36), other works could not observe these trapping sites after room temperature charging (Ref 37). The individual effects of strain rate and temperature were investigated recently by Finfrock et al. (Ref 38). They found that the heat generated during plastic deformation has less time to dissipate with increasing strain rate. Increasing the temperature increases the local chemical driving forces for hydrogen and carbon and decreases the probability of austenite transformation by the TRIP effect. Furthermore, Finfrock et al. (Ref 39) showed that the strain rate affects the strain hardening rate and the ductility of Q&P steels.

The role of intrinsic hydrogen on the degradation of the mechanical properties of low carbon Mn-Si steels has mainly been studied by applying the slow strain rate test (SSRT) method (Ref 5, 6, 25, 40-42). The strain rates applied were around 10^{-5} s^{-1} or higher. Wang et al. (Ref 24) used, e.g., an initial strain rate of 10^{-3} s^{-1} to investigate the role of inter-lath austenite nanofilms as a potential remedy for HE. However, the hydrogen charging procedures were not consistent, and the charging times ranged from 5 min up to 40 h aiming to reach homogenous hydrogen distributions inside the specimens. The time between hydrogen charging and SSRT was also different, which may cause hydrogen desorption (Ref 32). Thus, the interaction of hydrogen and RA in Q&P steels needs more detailed investigation.

As stated above, heat-treated low carbon Mn-Si Q&P steels normally have multiphase microstructures composed of tempered martensite and RA. A few studies focused on the intrinsic susceptibility to HE (Ref 13, 25, 41-45) by applying SSRT after charging. To the author's knowledge, the extrinsic susceptibility of Q&P steels to HE has not been investigated. Therefore, the present work aims to study the role of the Q&P heat treatment on the mechanical properties of 20Mn-Si steel. The susceptibility to HE is measured by incremental step load testing (ISLT) (Ref 41-43) according the ASTM F1624-12 standard. For that purpose, a recently developed electrochemical cell was attached to a tensile testing machine, which enabled continuous in situ hydrogen charging during stepwise mechanical loading. The

testing time was up to 60 h. After ISLT, detailed microstructure characterization was performed on the specimens to elucidate the nature of the RA phases in the Q&P steel.

2. Experimental Procedure

2.1 Material and Heat Treatment

20Mn-Si steel containing 0.2 wt.% carbon, 2.5 wt.% manganese and 1.5 wt.% silicon was investigated. The steel was produced by voestalpine Wire Rod GmbH in a laboratory vacuum-induced melting unit. The steel was cast and machined into rods with a diameter of 12 mm and length of 200 mm, which are named "as-delivered" throughout the following text.

Q&P heat treatments, as schematically illustrated in Fig. 1 (Ref 46, 47), were applied to the 20Mn-Si steel. For that purpose, the as-delivered rods were austenitized in a vacuum retort furnace at 900 °C for 30 min and subsequently quenched to the temperature T_Q using a salt bath. Afterward, the partitioning process was performed by heating the salt bath together with the rods to the partitioning temperature T_P in a furnace. Finally, the rods were water quenched to room temperature. The relevant Q&P process parameters are summarized in Table 1.

Dilatometer studies were conducted to measure the martensite start temperature M_S and the martensite finish temperature M_F. Basically, rapid quenching to T_Q, which is located between M_S and M_F, determines the volume fraction of RA in the 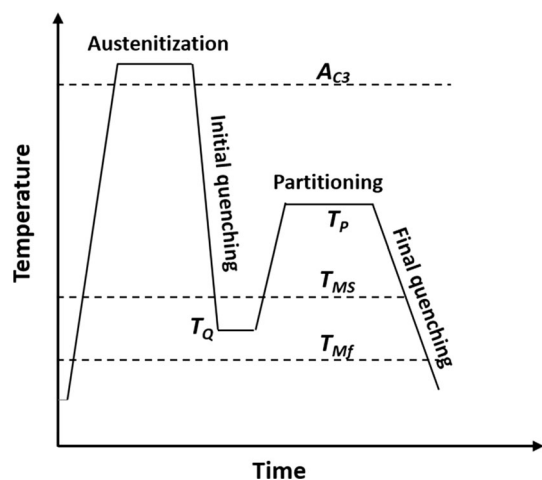microstructure. A Bähr 805 A/D dilatometer with helium gas atmosphere was used for that purpose. Cylindrical specimens were machined out of the as-received rods with a diameter of 4 mm and length of 10 mm. The transformation temperatures were determined by measuring the extension u of the sample during heating and subsequent cooling. The transformation temperatures were determined using a tangent at the beginning of the phase transition according to ASTM A 1033–04 standard. Furthermore, the Q&P heat treatments were experimentally simulated to study the phase transformations qualitatively.

2.2 Mechanical Characterization

Mechanical properties according to the ASTM E8 standard were measured using an electromechanical ZwickRoell Kappa 250 DS tensile testing machine. The tensile tests were conducted with a 1 mm/min displacement rate. Dog bone-shaped tensile specimens, according to DIN 50,125-A, were used. The gauge length was 30 mm, and the gauge diameter was 5 mm. Specimens were machined out of Q&P heat-treated rods with the specimen axis parallel to the rod axis or the rolling direction. In addition, Vickers hardness measurements on the heat-treated Q&P steels were performed using an EMCO-TEST hardness tester equipped with a pyramidal diamond cone and a weight of 10 kg. The hardness values reported in this work were averaged from the values of five measurements made along the diameter of the rod.

2.3 Microstructure Characterization

The microstructure of the specimens after Q&P heat treatment was analyzed on different length scales to identify phases and phase distributions. Light optical microscopy (LOM), scanning electron microscopy (SEM), and electron back-scattered diffraction (EBSD) were applied after cutting, grinding and polishing the specimens. The microstructures were revealed by etching the polished surface with 3 vol.% Nital solution for 30 s in the case of LOM and only 3 s for SEM and EBSD. Nital etching turns ferritic areas into white, while pearlitic or martensitic areas appear brown (Ref 48). LOM investigations were performed using a Zeiss Axio Observer Inverted microscope, and SEM investigations were performed using a Tescan Mira 3 microscope equipped with an electron back-scattered diffraction (EBSD) Hikari detector and a TSL-OIM software package for data analysis. EBSD measurements were carried out at the area of $50 \times 50 \ \mu m^2$ using the acceleration voltage of 30 kV and the spot size of 54 nm.

In addition, transmission electron microscopy (TEM) was performed to identify the distribution and morphology of RA. For that purpose, a JEOL 200CX microscope operated at the acceleration voltage of 200 kV and a Phillips CM 300

Fig. 1 Sketch of the Q&P heat treatment process with an indication of the relevant parameters

Table 1   Q&P processing parameters

Specimen/Q&P heat treatment	Quenching temperature T_Q, °C	Quenching time t_Q, s	Partitioning temperature T_P, °C	Partitioning time t_P, s
QP1	235	120	390	1800
QP1_t	235	10	390	420
QP2	290	120	370	1800
QP2_t	290	10	370	420

microscope operated at the acceleration voltage of 300 kV were used. Selected area electron diffraction (SAED) was used to identify the phases. TEM investigations were applied on small disks with a diameter of 3 mm and thickness of about 0.1 mm. The disks were jet-electropolished in electrolyte HNO_3:-$CH_3OH = 3{:}7$ at 0 °C and 15 V to obtain transparent areas near the central hole.

X-ray diffraction (XRD) patterns were recorded for each of the applied Q&P heat treatments using a Bruker D8 Advance powder diffractometer with a Cu Kα x-ray source. XRD measurements were performed in the range of 40-85° 2θ with a step size of 0.02° and a counting time of 5 s per step. The volume fraction of RA f_{RA} was evaluated from the XRD patterns by TOPAS software using the Rietveld method for spectra analysis (Ref 49). Each specimen was carefully prepared for XRD analysis to minimize the influence of RA transformation in near-surface regions due to specimen preparation.

2.4 Hydrogen Charging and Thermal Desorption Analysis

Specimens with a diameter of 5 mm and length of 20 mm were electrochemically charged with hydrogen using 3.5 vol.% NaCl solution with 0.1 vol.% thiourea (CH_4N_2S) as a hydrogen recombination inhibitor. The cathodic polarization voltage was maintained at -1.1 V against an Ag\AgCl reference electrode using a dimensionally stable anode (DSA) and a potentiostat with an accuracy of 0.2%. Electrochemical hydrogen charging of the specimen did not cause any internal material damage (Ref 50). Hydrogen charging was applied for 24 h. After charging, the specimens were cleaned and dried with compressed air.

Thermal desorption analysis (TDA) was applied to measure the hydrogen content after electrochemical charging using a Bruker Galileo G8 analyzer equipped with a mass spectrometer. Transportation from the electrochemical cell to the thermal desorption analyzer took less than 3 min to minimize desorption's influence on the measured hydrogen content. No additional evacuation was necessary before starting the measurements. For thermal desorption, charged specimens were
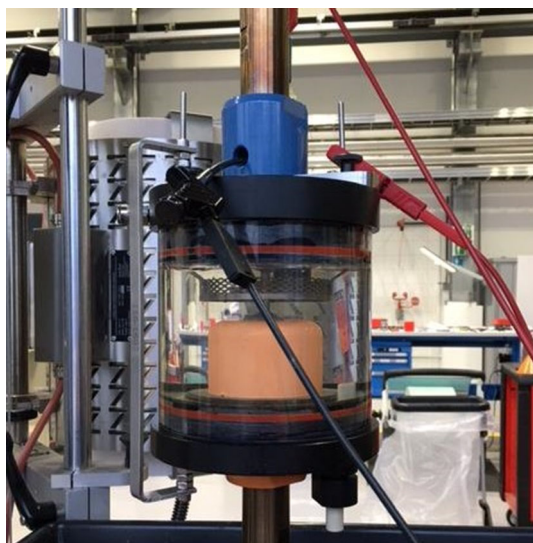

Fig. 2 Electrochemical cell for in situ hydrogen charging applied to an electromechanical tensile machine

heated within an infrared furnace and a heating rate of 0.32 °C/s to 900 °C.

2.5 Incremental Step Load Testing (ISLT)

The resistivity to HE was evaluated by comparing the ultimate tensile strength R_m measured in air and measured by ISLT during in situ charging of the specimens. For that purpose, the electromechanical tensile testing machine was equipped with a recently developed electrochemical cell, as presented in Fig. 2. This cell enables continuous hydrogen absorption by cathodic polarization of the specimen surface during ISLT. Before testing, the specimens were polished with steel wool, flushed well with distilled water, and degreased with acetone or ethanol. The specimens were kept dry until starting the test.

The ASTM F1624-12 standard recommends ISLT according to the loading protocol (10\5\2,4) for steels with hardness between 310 HV10 to 448 HV10. Therefore, the applied load maximum was divided into 20 steps with a 5% load increase per step. In the first test, the maximum load was set equal to the ultimate tensile strength. In each of the following tests, the maximum load was set equal to $1.1P_{th}$, with P_{th} being the threshold force of the last completed step before reaching the fracture force. This procedure decreased the loading rate, enhancing the measurements' accuracy. The holding time in each of the first ten steps was 2 h. After the tenth step, the holding time was increased to 4 h. Normally, 3 to 4 specimens should be tested for each material until two consecutive tests reach a fracture strength within the test accuracy of 5% of the ultimate tensile strength (Ref 51-53). According to ASTM F1624-12 standard, the threshold stress σ_{th} is calculated from the lowest threshold force P_{th} as

$$\sigma_{th} = \frac{P_{th}}{A_0} \tag{Eq 1}$$

where A_0 is the initial cross-sectional area of the specimen. The threshold stress represents the stress below which HE will never occur for a given hydrogen charging condition (Ref 54). In addition, the relative susceptibility embrittlement index EI representing the percentage drop in the tensile strength due to hydrogen uptake and can be calculated as

$$EI = 100 \cdot \left(1 - \frac{\sigma_H}{R_m}\right) \tag{Eq 2}$$

where σ_H is the fracture stress in the hydrogen donating atmosphere. Furthermore, the average strain rate $\bar{\dot{\varepsilon}}$ of the ISLT can be calculated in the elastic regime as follows:

$$\bar{\dot{\varepsilon}} = \frac{1}{t}\left(\frac{\sigma_{th}}{E}\right) \tag{Eq 3}$$

with t being the time to crack initiation and E being Young's modulus of 210 GPa. Equation 3 allows a rough comparison of strain rates applied in the present ISLT with the SSRT performed in the literature.

3. Results and Discussion

3.1 Tensile Testing and Hardness Measurements

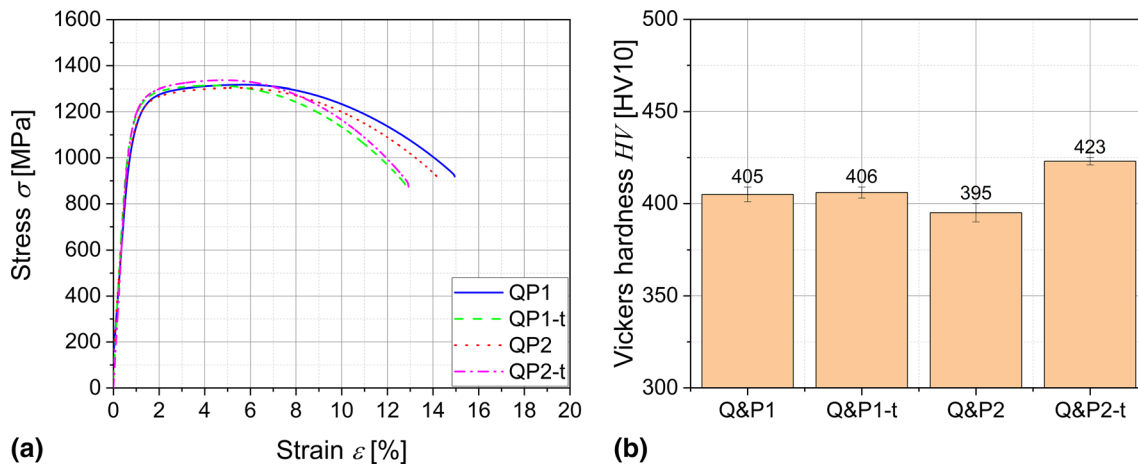Representative stress–strain curves determined for each Q&P heat treatment are shown in Fig. 3(a), and the corre-

Fig. 3 (a) Tensile curves and (b) averaged Vickers hardness of Q&P heat-treated materials

Table 2 Mechanical properties of Q&P heat-treated steel

Specimen/Q&P heat treatment	Ultimate tensile strength R_m, MPa	Fracture elongation A_l, %	Vickers hardness HV, HV10	Threshold stress σ_{th}, MPa	Embrittlement index $EI_{-1.1V}$, %
QP1	1317 ± 12	15.2	405 ± 4	833	35.5 ± 4
QP1-t	1314 ± 10	12.8	406 ± 3	650	47.5 ± 2
QP2	1314 ± 10	14.5	395 ± 5	850	30 ± 5
QP2-t	1337 ± 10	12.9	423 ± 2	560	54.5 ± 2

sponding mechanical properties are listed in Table 2. The ultimate tensile strength is similar for the different Q&P heat treatments, with the highest strength of 1337 MPa for QP2-t. The other samples, QP1, QP1-t and QP2, have almost the same ultimate tensile strength, which confirmed the identical hardness measured at the cross sections of the rods, Fig. 3(b). The ductility gain due to the Q&P heat treatments was evaluated by examining the fracture elongation. The highest and lowest fracture elongation of 15.2 and 12.8% were measured for QP1 and QP1-t, respectively. Fracture elongation of 14.5% (QP2) decreases with decreasing partitioning time to 12.9% (QP2-t). Obviously, the decrease in partitioning time or temperature also decreases fracture elongation. For Q&P heat-treated Fe-C-Mn-Si steels, Kaar et al. (Ref 55) showed that volume fractions of 80-90 vol.% of martensite result in ultimate tensile strength of 1320 MPa and in fracture elongation of 14%, which are both very similar than the properties of the present steel. Microstructure evolution had less effect on the ultimate tensile strength than on the fracture elongation, which agrees with the present results.

3.2 Retained Austenite Characterization

Besides the magnetization technique (Ref 6, 26), XRD is the most common technique for quantifying the volume fraction of RA in Q&P steels (Ref 37, 41, 56). Figure 4(a) shows the measured XRD patterns of Q&P heat-treated specimens. Six peaks occur in the measured diffraction pattern. Three peaks belong to the body-centered tetragonal (bct) martensitic crystal structure, and three belong to the face-centered cubic (fcc) RA crystal structure. The volume fractions of RA evaluated for each of the Q&P heat treatments range from 8.1 to 13.2%, as summarized in Fig. 4(b). Basically, the measured values are in

good agreement with values given in the literature for Q&P steels (Ref 5, 6). The martensite reaction is usually athermal during quenching, and the corresponding volume fraction depends on the undercooling $\Delta T = M_s - T_Q$ below martensite start temperature and not on time. According to the Koistinen–Marburger (KM) relationship f_{RA} can be calculated as

$$f_{RA} = \exp\big(\beta\big(M_S - T_Q\big)\big) \qquad \text{(Eq 4)}$$

where β is a fitting coefficient of around -0.011 K^{-1} (Ref 57), assuming complete carbon partitioning from the martensite to the austenite phase. According to the measurements in Fig. 4(b), an estimation of β revealed $-0.017\ K^{-1}$ and $-0.032\ K^{-1}$.

3.3 Phase Transformation Temperature

Figure 5(a) shows the recorded dilatometer curve of the austenitization and quenching step. The critical austenite start temperature A_{c1} and austenite finish temperature A_{c3} were determined as 745 and 850 °C, respectively, by applying a tangent near the start of the phase transition. The martensite start temperature M_s and martensite finish temperature M_f were determined as 359 and 230 °C, respectively. Thus, quenching after full austenitization below the M_s causes martensite formation. Comparing the measured M_s with the prediction of $M_s = 354\ °C \pm 8.5\ °C$, according to Kaar et al. (Ref 58), gives almost perfect agreement. Since M_f is much higher than room temperature, quenching to room temperature would form a fully martensitic microstructure. However, during the partitioning step, carbon diffuses from martensite to the remaining austenite, which decreases the martensite start temperature and stabilizes the RA phases at room temperature. As shown in Fig. 5(b), further dilatometer tests were conducted to measure
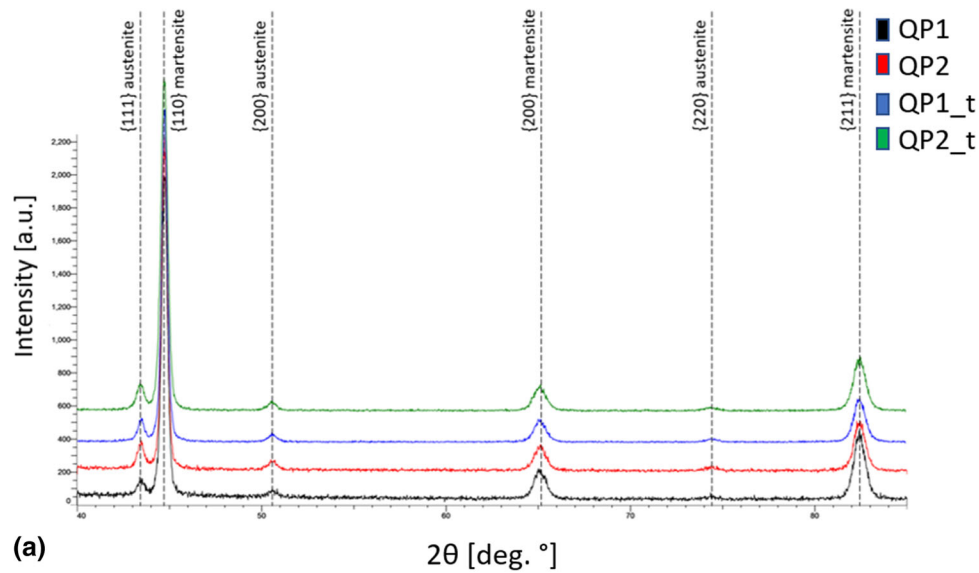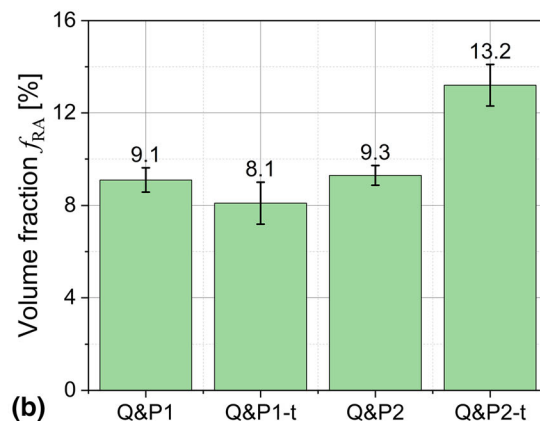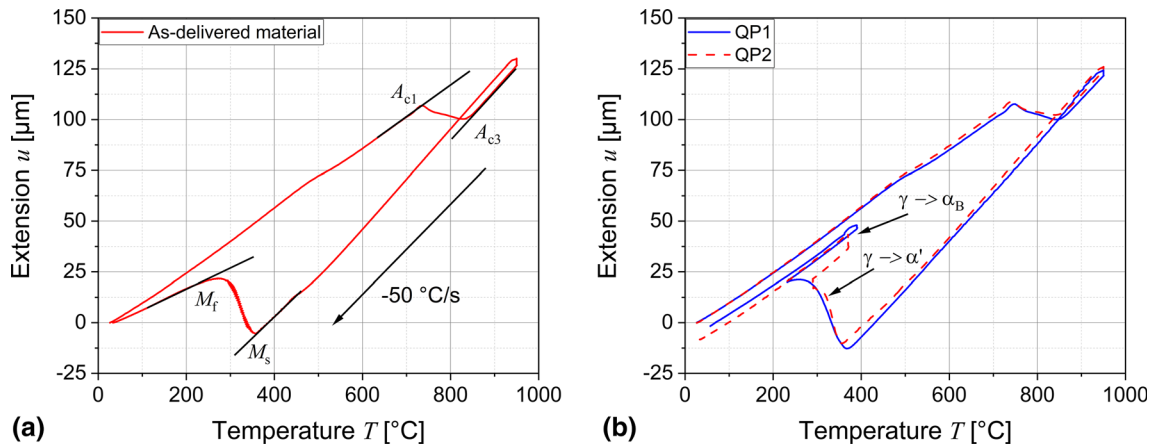
Fig. 4 (a) Measured XRD patterns of the Q&P steels and (b) corresponding volume fractions of RA

Fig. 5 Dilatometric curves recorded during (a) austenitization and quenching and (b) during QP1 and QP2 heat treatments

the dilatation during the QP1 and QP2 heat treatments. After austenitization at 950 °C for 600 s, the specimens were quenched with the cooling rate of −50 °C/s, held at the quenching temperature of 235 °C or 290 °C for 30 s, and reheated to the partitioning temperature of 390 °C or 370 °C for QP1 and QP2, respectively. After successive partitioning for

600 s, the specimens were finally cooled to room temperature. The dilatometry results show that besides transformation of austenite γ to martensite α' during first quenching, there is also decomposition of RA to bainitic ferrite α_B during isothermal partitioning slightly above M_s. The extension u during partitioning was larger for QP2 than for QP1, even though
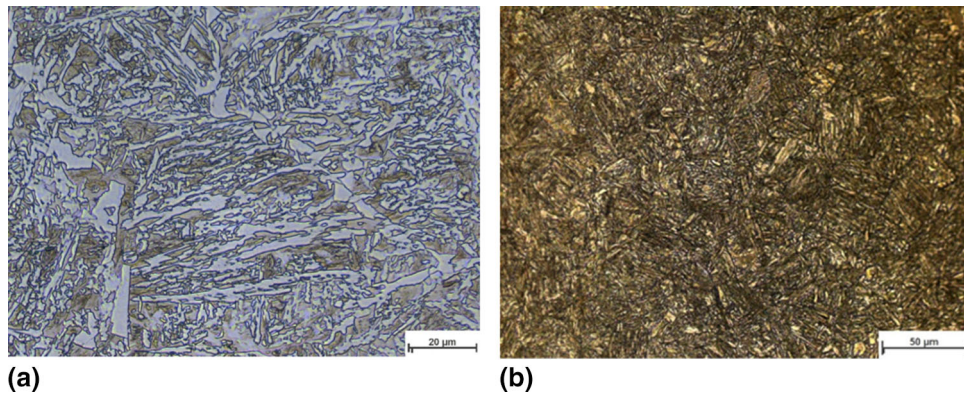
Fig. 6 Representative micrographs of Nital etched (a) as-received and (b) heat-treated (QP1) steel
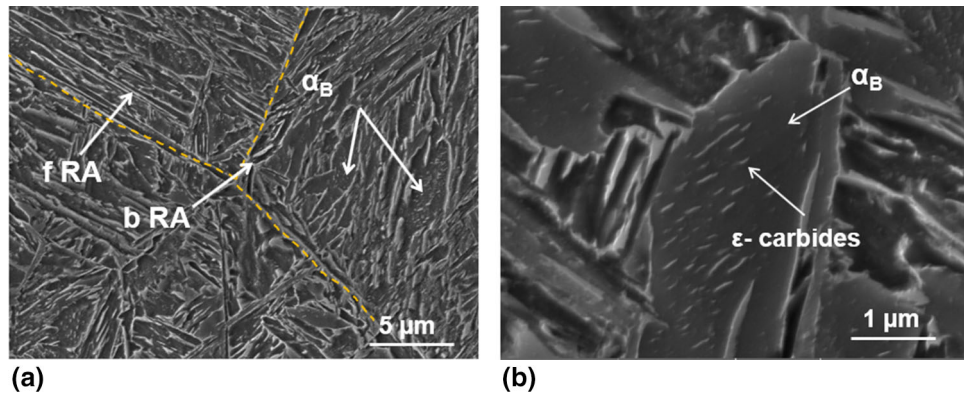

Fig. 7 Representative SEM micrographs of the Q&P microstructure with (a) lower and (b) higher magnifications
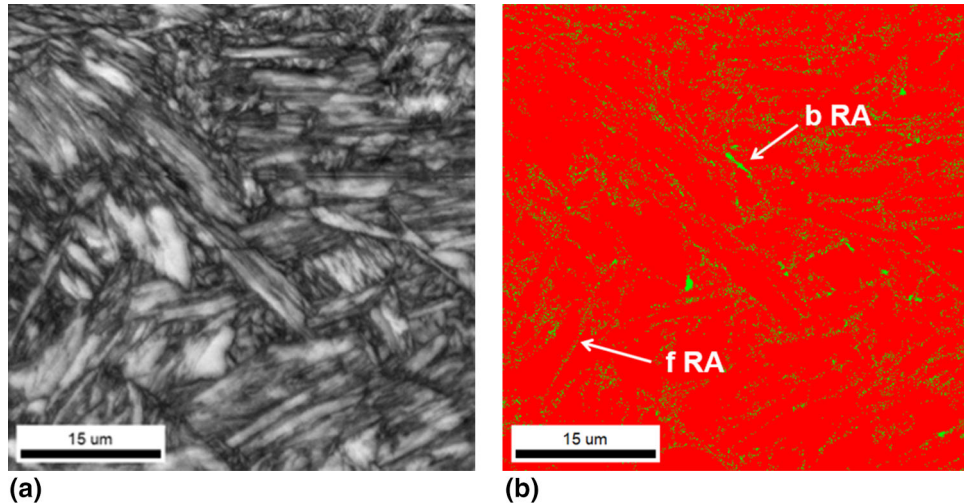

Fig. 8 EBSD characterization of the Q&P microstructure: (a) image quality and (b) phase map (red: bcc phase, green: fcc RA phase) (Color figure online)

the partitioning times were equal. This agrees with larger volume fractions of bainitic ferrite found by Kaar et al. (Ref 55) for lower primary martensite α' and thus for lower quenching temperatures. The curves do not show further significant dilatation during final cooling to RT, which would indicate a formation of fresh and untempered martensite (Ref 59).

3.4 Microstructure Characterization

For characterizing the microstructures of the as-delivered material and after QP heat treatment, Nital etching was applied, and micrographs were taken using LOM. As shown in Fig. 6(a), the as-received material has a pearlitic-ferritic microstructure. Needle-like ferritic grains with blocky pearlitic
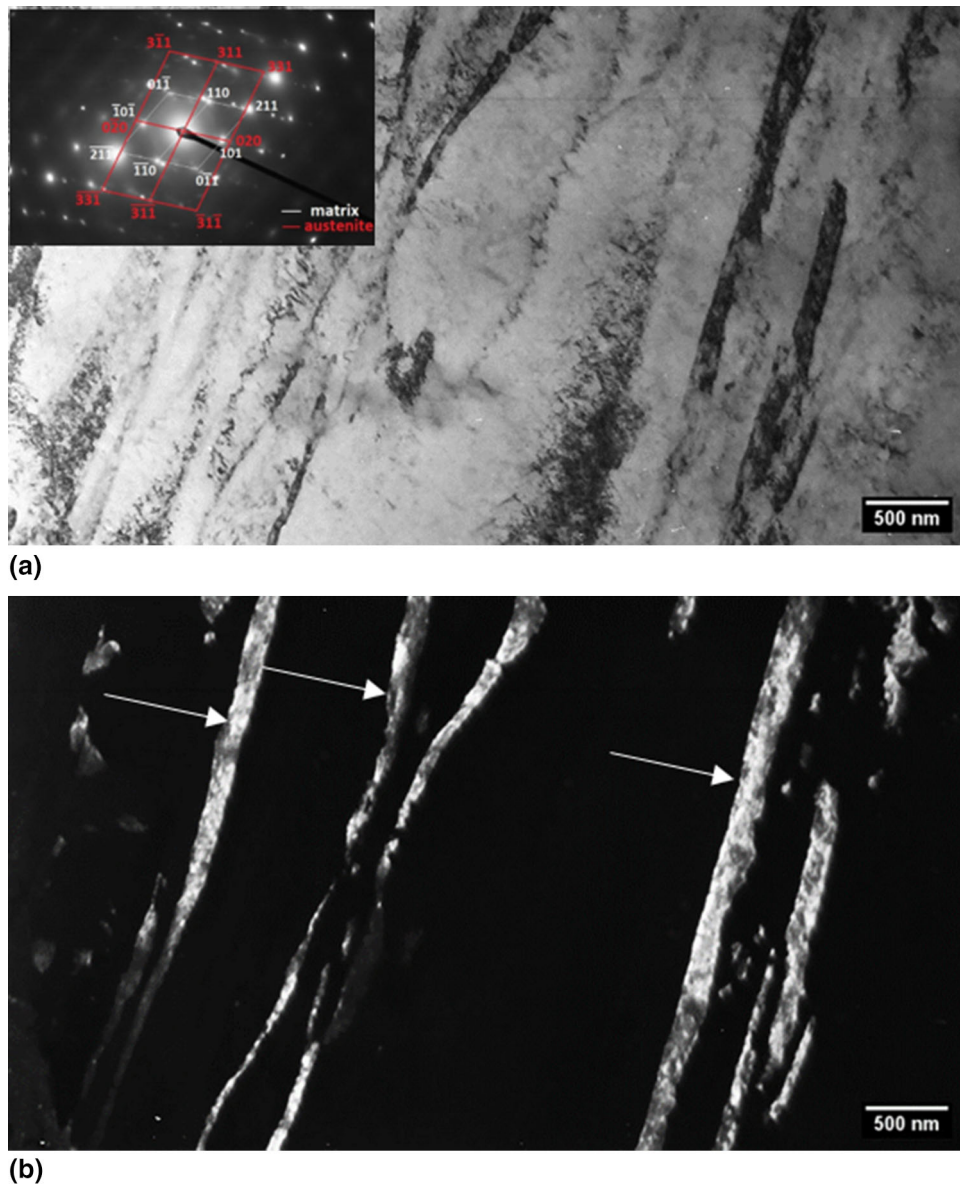
(a)

(b)

Fig. 9 (a) Bright-field TEM micrograph with electron diffraction pattern of the matrix and retained austenite and (b) dark-field TEM micrograph of the same position

areas in between occur. Nital etching of the steel after QP heat treatment reveals the martensitic matrix, as shown in Fig. 6(b).

Figure 7(a) shows corresponding SEM images consisting of a matrix of ultra-fine-grained tempered martensite and some bainitic ferrite with finely dispersed RA. The volume fraction of bainitic ferrite in Fe-C-Mn-Si steels is about 5-15 vol.%, as estimated by Kaar et al. (Ref 55). The morphology of RA between the martensitic laths is either blocky (b RA) or filmy (f RA). The prior austenite grain boundaries are marked with yellow dashed lines. The higher magnification in Fig. 7(b) reveals some bainitic ferrite with precipitates, which are likely epsilon carbides ε (Ref 60) or cementite.

Representative EBSD measurements for studying the distribution and morphology of RA within the martensitic matrix were performed at the cross sections of the rods. Figure 8(a) shows the image quality, which corresponds with the local defect density. Bright areas of low defect density are surrounded by comparatively dark areas of high defect density

(martensite). The corresponding phase map in Fig. 8(b) shows mainly thin films of RA (f RA) between martensite laths, and some blocks of RA (b RA) were also found. f_{RA} evaluated by EBSD was < 2 vol.% for each of the four heat treatment conditions, which is much less than f_{RA} measured by XRD of > 7.4 vol.%. The higher surface sensitivity of EBSD compared to XRD or magnetization methods commonly leads to an underestimation of f_{RA}. Therefore, e.g. surface deformation during specimen preparation may influence the results of EBSD measurements.

The results of TEM measurements confirm the findings of EBSD measurements. Figure 9(a) and (b) shows bright and dark-field images, respectively. The presence of thin RA films (white bands in Fig. 9b) at the boundaries of the martensitic laths was confirmed by electron diffraction patterns (small image in the corner of Fig. 9a). The thickness of the RA films was about 100 nm.
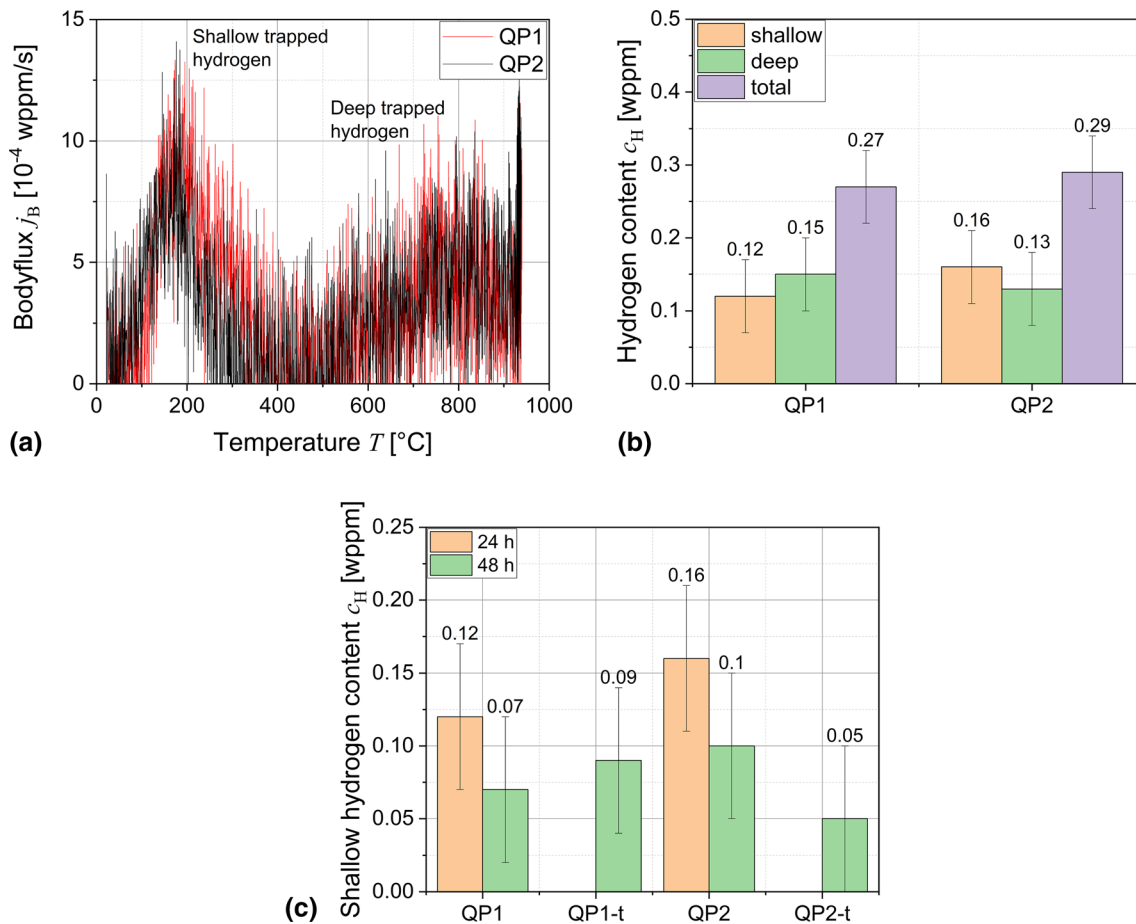
Fig. 10 Hydrogen uptake and trapping characteristics of QP1 and QP2: (a) TDA spectra and (b) corresponding hydrogen contents.(c) Shallow hydrogen content after 24 h and 48 h of hydrogen charging

3.5 Hydrogen Analysis

The hydrogen uptake after 24 h of electrochemical charging was evaluated for QP1 and QP2 heat-treated specimens, which contain almost similar f_{RA} of 9.1 vol.% and 9.3 vol.%, respectively. The recorded TDA spectra are shown in Fig. 10(a). The spectrum consists of two peaks, a shallow-trapped hydrogen peak and a deep-trapped hydrogen peak. The areas below the peaks correspond to the hydrogen contents. As shown in Fig. 10(b), the shallow hydrogen content of QP1 and QP2 is 0.12 wppm and 0.16 wppm, respectively. The deep-trapped hydrogen content and thus also the total hydrogen content are almost equal for QP1 and QP2 with 0.3 wppm.

The shallow-trapped peaks range from room temperature to 400 °C with maxima at 180 °C for QP1 and 170 °C for QP2. This is also in agreement with Lovicu et al. (Ref 5), who compared TDA spectra after Q&P heat treatment and after quenching and tempering (Q&T) heat treatment. The shallow-trapped peak shifted from 170 °C (QP2) to 180 °C (QP1), which is most likely caused by the larger number of trapping sites in the martensitic matrix rather than by the increase in the trapping energy (Ref 34). The higher partitioning temperature may cause slightly enhanced recovery during QP1 than during QP2, which may reduce the trap density in the QP1 heat-treated microstructure.

In addition, a deep-trapped hydrogen peak was measured at a higher temperature. This differs from measured TDA spectra

showing only single peaks (Ref 5, 24). For example, Lovicu et al. (Ref 5) measured only a single TDA peak for Mn-Si steels with f_{RA} more than twice as in the present steel. They found that the effect of austenite on hydrogen trapping results in slight enlargement and shift of the peak toward higher temperature, rather than causing an additional peak at high temperature. However, deep-trapped hydrogen peaks are generally more difficult to interpret because heating to higher temperatures causes microstructure evolution and phase transformation. To the authors' knowledge, both of these effects are currently not considered in any TDA interpretation. Furthermore, Lin et al. (Ref 61) and Hitzigrath (Ref 62) showed that thermal dissociation of water molecules at the surface likely causes additional hydrogen evolution, which can explain considerable tailing of the flux during long-lasting high-temperature measurements. Due to these overlaying effects, distinguishing hydrogen molecules from the surface and bulk is challenging at high specimen temperatures.

To study the effect of retained austenite volume fraction on the shallow-trapped hydrogen content, additional measurements were performed after 48 h of charging, as shown in Fig. 10(c). Although the hydrogen content was slightly smaller compared to 24 h of charging, the values were in the range of the scatter band. The shallow hydrogen content seems not to correlate with the RA volume fraction, which supports the hypothesis of trapped hydrogen in the martensitic matrix or at the RA interface.
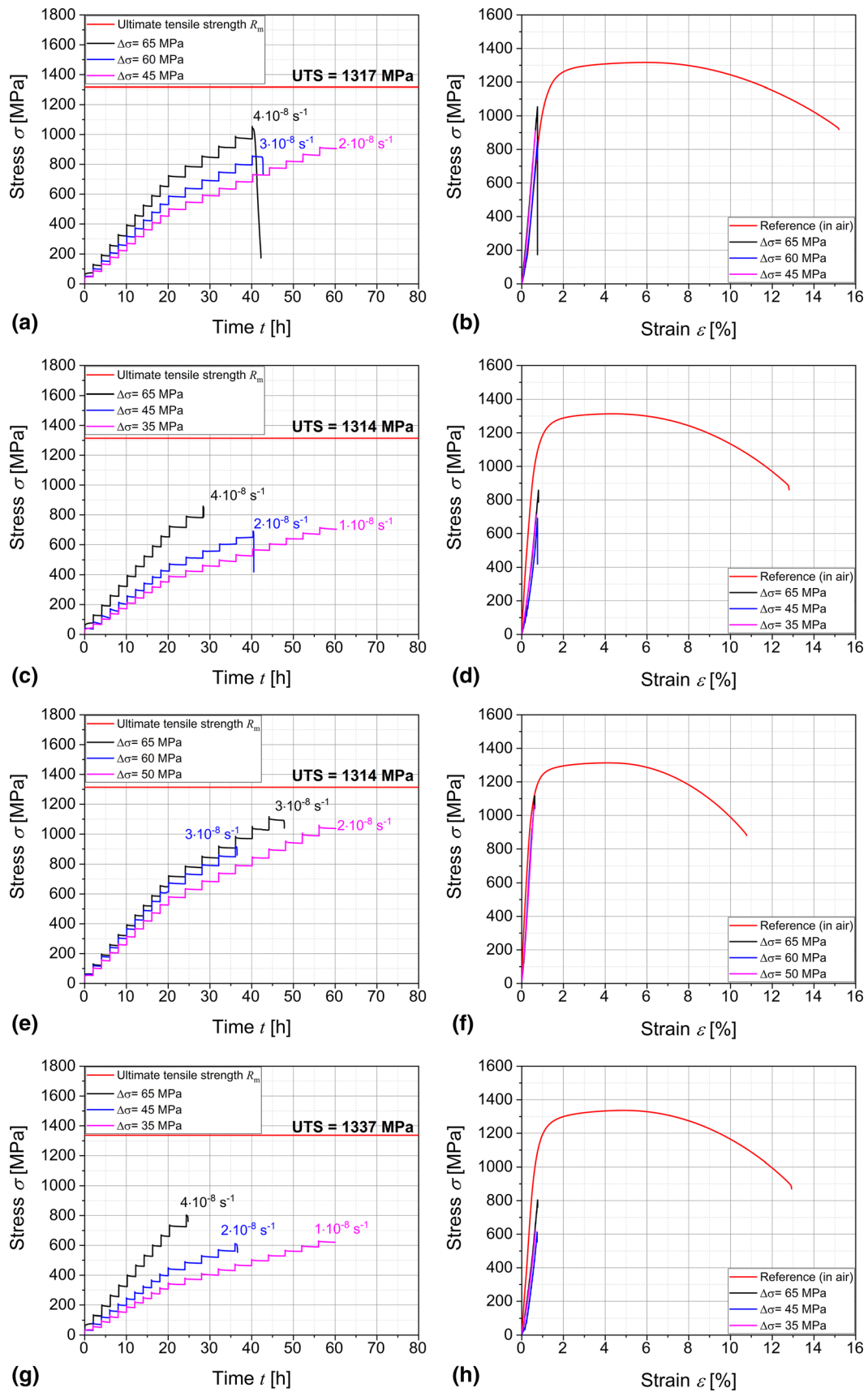
Fig. 11 (a), (c), (e), (g) ISLT curves and (b), (d), (f), (h) quasi-static stress–strain curves for 20Mn-Si steel after QP1 (a and b) QP1-t (c and d), QP2 (e and f) and QP2-t (g and h)

3.6 Incremental Step Load Testing

ISLT with continuous hydrogen uptake during loading was applied to evaluate the HE relative resistivity of Q&P heat-treated 20Mn-Si steel rods. The recorded stepwise increasing stress-time curves and the corresponding stress–strain curves are given in Fig. 11. For each heat treatment, ISLT took up to seven days using three specimens. The corresponding average strain rates $\bar{\varepsilon}$ according to Eq. (3) are given next to the fracture strengths in Fig. 11(a), (c), (e), and (g) for QP1, QP1-t, QP2 and QP2-t, respectively. The higher the average strain rate, the higher the fracture strength reached within ISLT. The threshold stress is reached in recent work for average strain rates lower than $2 \cdot 10\text{-}8 \ s^{-1}$. Drexler et al. showed theoretically that strain rates below $10^{-7} \ s^{-1}$ are necessary in the case of deep trapping sites to reach quasi-static diffusion conditions during mechanical loading (Ref 9).

In Fig. 11(b), (d), (f), and (h), corresponding stress–strain diagrams are plotted for QP1, QP1-t, QP2 and QP2-t, respectively. It is obvious that each hydrogen-charged specimen fractured without macroscopic plastic straining before reaching the yield point. The highest threshold stress of 850 MPa was obtained by QP2, while lower threshold stresses of 650 MPa and 560 MPa were obtained by QP1-t and QP2-t, respectively. Therefore, QP2-t resulted in the highest embrittlement index *EI* of 54.5%, representing the highest loss in tensile strength due to the effect of hydrogen absorption. *EI* of QP1-t, QP1 and QP2 were 47.5, 35.5 and 30%, respectively. The ISLT results are listed in Table 2. The results show that a long partitioning time is necessary for good performance, which can be attributed to carbon segregation to RA causing local stabilization of the microstructure. QP2 shows better performance than QP1, most likely due to quenching to a higher temperature causing the formation of more bainite volume fraction.

Figure 12 shows the representative fracture surface of a QP1-t specimen imaged using SEM after ISLT. The fracture surfaces of the other QP heat-treated specimens were all similar. As shown in Fig. 12(a), cracking started at the lower right-hand side and propagated to the upper left-hand side. Cracking started with brittle intergranular fracture mode (Ref 63), as indicated by the open grain boundaries in Fig. 12(b). Mixed intergranular (IG) and quasi-cleavage (QC) fracture modes with ductile dimple pockets occurred at the center of the cylindrical specimen, as shown in Fig. 12(c). Finally, a ductile fracture mode characterized by dimples and microvoids, as shown in Fig. 12(d), occurred. Basically, the observed change in the fracture mode agrees with the work of Beachem (Ref 64, 65), who proposed a qualitative diagram of critical combinations of threshold stress intensity K and hydrogen content c_H for each fracture mode. With increasing K at given c_H, the fracture mode changes from IG over QC to microvoid coalescence (MVC).

The fracture mode with mainly IG crack initiation and propagation along the prior austenite grains (PAG) supports the postulations of mixed HELP and HEDE mechanisms as discussed by M. Djukic et al. (Ref 23) and J. Rehrl et al. (Ref 66). Rehrl et al. postulated that the characteristic features of the HE fracture are due to hydrogen transport by dislocation to the fracture process zone and that this transportation is not possible when the dislocation motion exceeds a certain level. This is why these features do not exist while using a fast strain rate. However, the slowest strain rate used in their investigation was $10^{-5} \ s^{-1}$. In the recent work, the ISLT with the loading protocol (20/5/2,4) has a slower strain rate down to $10^{-8} \ s^{-1}$, which is much slower and gives a chance to transition from MVC into IG mode.

As shown in Fig. 13(a), both the threshold stress as well as the corresponding fracture stress reached at the higher average
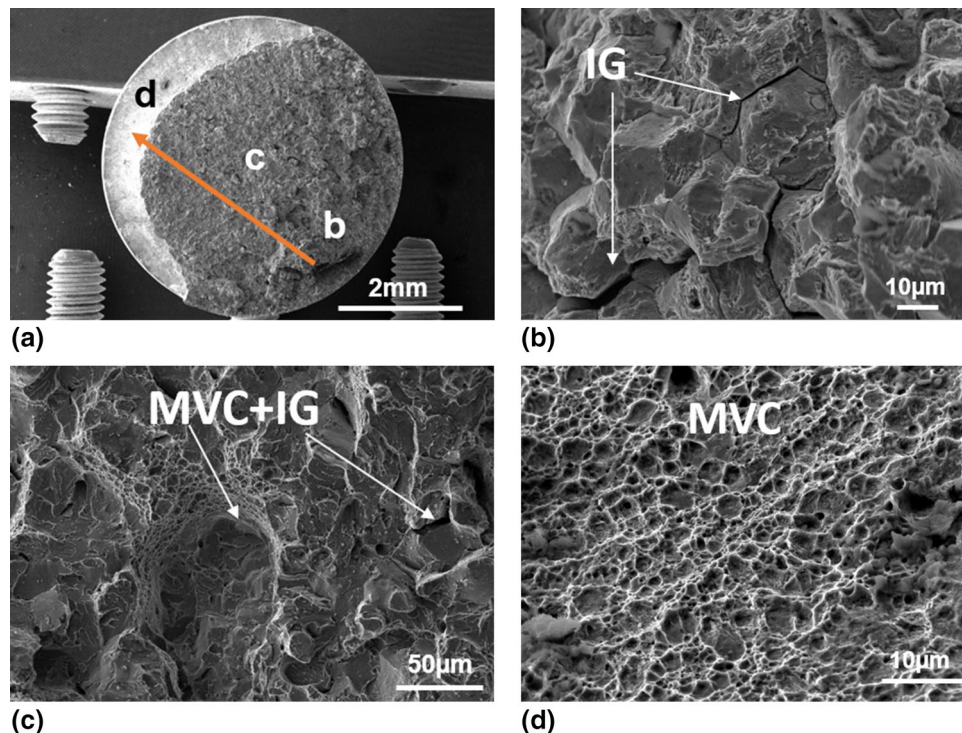

Fig. 12 Representative fracture surface analysis after incremental step load testing of QP1-t specimen: (a) overview image and detailed images of areas (b), (c) and (d)
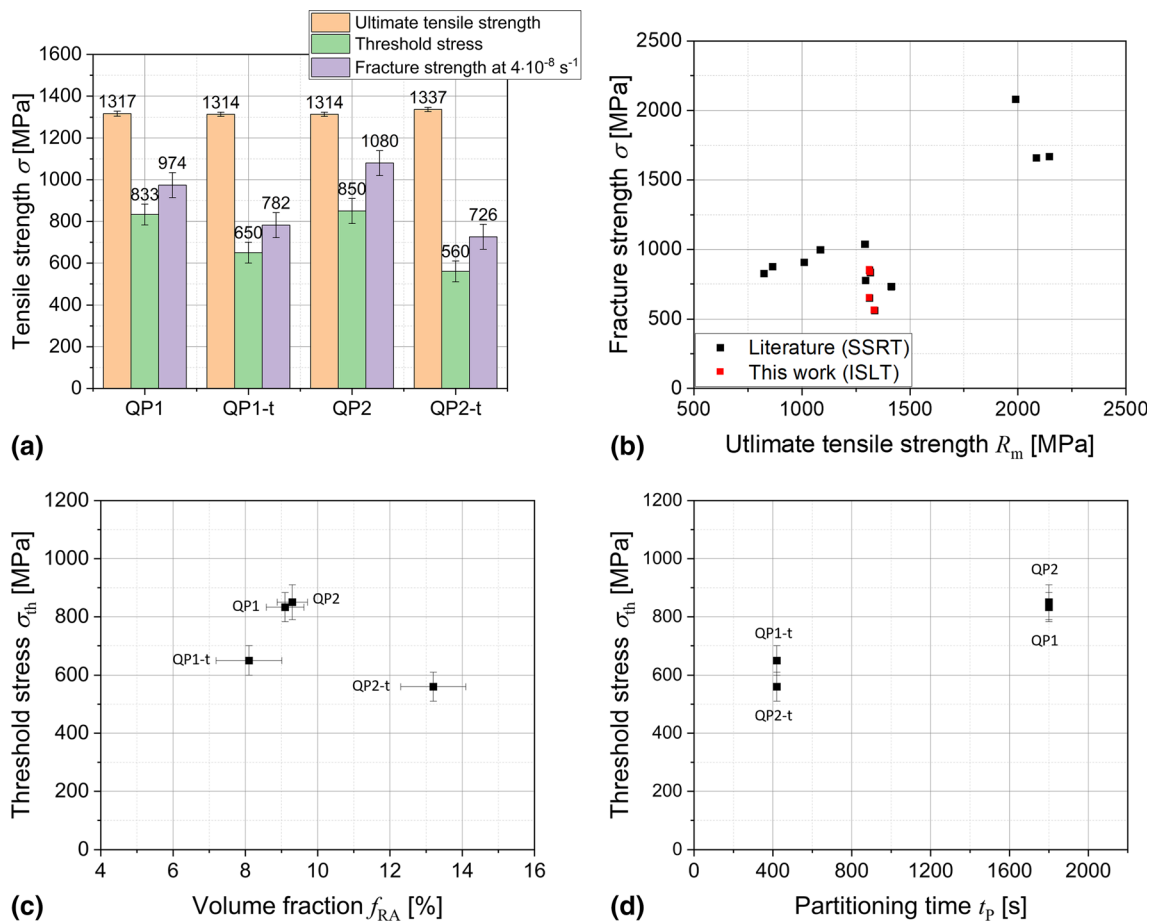
Fig. 13 (a) Fracture strengths measured for different Q&P heat treatments. (a) Fracture strength as function of ultimate tensile strength (Ref 6, 25, 40-42, 67). Correlation between threshold stress and (c) retained austenite volume fraction and (d) partitioning time

strain rate of $4 \cdot 10^{-8}$ s^{-1} follow almost identical trends, with QP2 performing best under a hydrogen donating environment. This would allow for reducing the total testing time from seven days to around 48 h and for minimizing the number of specimens to only one. Such a simplified procedure can be used, for example, for fast material screening or optimizing heat treatment parameters.

In Fig. 13(b), the threshold stresses for each of the three Q&P heat treatments are compared with fracture stresses published in the literature, which were only determined in SSRT at relatively high strain rates above 10^{-5} s^{-1} and using precharged specimens (Ref 6, 25, 40-42, 67). Obviously, the strain rate is crucial as it affects the fracture strength of hydrogen-containing specimens. Fracture strengths published in the literature are higher than the measured threshold stresses. As shown in Fig. 11, the ISLT specimens tested in the present work fractured within the linear elastic regime, whereas Q&P heat-treated specimens investigated in the literature showed some plastic yielding (Ref 41).

In Fig. 13(c), the correlation between threshold stress and RA volume fraction shows no clear trend, with a maximum in the threshold stress at around 9%. However, comparing the threshold stress with the partitioning time, as shown in Fig. 13(d), reveals a linear correlation. Increasing the partitioning time increases the threshold stress dramatically by approximately 200 MPa, which supports the hypothesis that long-time carbon partitioning causes RA stabilization.

In the present work, the ISLT specimens fractured below the macroscopic yield point and thus without any macroscopic plastic deformation. However, the composite-like microstructure of Q&P heat-treated steels causes inhomogeneous stress distribution between "hard" martensite and "soft" RA. Load is mainly carried by martensite phases. Thus, microscopic yielding is likely to occur in the RA even before reaching the macroscopic yield point. This may trigger local transformation to untempered martensite in the presence of hydrogen.

4. Summary and Conclusions

The present work investigates the influence of different Q&P heat treatments on the HE susceptibility of 20Mn-Si steel rods. For that purpose, ISLT was performed in a hydrogen donating environment under controlled conditions according to ASTM F1624-12 standard. Volume fractions of RA were measured by XRD after heat treatment. TDA was applied to measure the hydrogen content after charging. Microstructural characterization was performed on different length scales using LOM, SEM and TEM. The following results can be summarized:

- The Q&P heat-treated microstructures consist of a matrix of tempered martensite containing bainitic ferrite and RA,

which has mainly film-like morphology with an estimated thickness of about 100 nm.

- Measured volume fractions of RA are between 8.1 and 13.2 vol.%, depending on the Q&P heat treatment conditions. Martensite transformation occurs during quenching, but the isothermal transformation of RA to bainitic ferrite takes place during partitioning above the martensite start temperature.
- TDA spectra were recorded with a shallow and deep hydrogen peak. The measured shallow hydrogen contents were small and seemed not to correlate with the RA volume fraction. This supports the hypothesis of trapped hydrogen in the martensitic matrix or at RA interfaces.
- ISLT was performed to measure the threshold stress against HE for a specific hydrogen charging condition. For that purpose, a recently developed electrochemical charging cell was applied to the tensile testing machine. The QP2 heat-treated steel performs best with an ultimate tensile strength of 1314 MPa, a fracture elongation of 14.5% and threshold stress of 850 MPa.
- A correlation between the threshold stress and partitioning time was found, showing that the susceptibility of the QP2 heat treatment improved by 25% by increasing the partitioning time from 420 to 1800s. A clear influence of the retained austenite volume fraction on the threshold stress could not be confirmed.
- Comparing the threshold stresses with the fracture strengths measured at higher average strain rates revealed similar trends concerning the relative HE susceptibility. This observation can be used for reducing the overall testing time during material screening or for further optimization of Q&P heat treatment parameters.

Open Access

References

1. S. Keeler and M. Kimchi, Advanced High-Strength Steels Application Guidelines Version 5.0, *WorldAutoSteel*, 2014 https://doi.org/10.1016/S1644-9665(12)60197-6
2. J.G. Speer, E. De Moor, and A.J. Clarke, Critical Assessment 7: Quenching and Partitioning, *Mater. Sci. Technol. (United Kingdom)*, 2015, **31**, p 3–9. https://doi.org/10.1179/1743284714Y.0000000628
3. S. Kaar, R. Schneider, D. Krizan, C. Béal, and C. Sommitsch, Influence of the Quenching and Partitioning Process on the Transformation Kinetics and Hardness in a Lean Medium Manganese Trip Steel, *Metals (Basel)*, 2019 https://doi.org/10.3390/MET9030353
4. K. Steineder, D. Krizan, R. Schneider, C. Béal, and C. Sommitsch, On the Microstructural Characteristics Influencing the Yielding Behavior of ultra-Fine Grained Medium-Mn steels, *Acta Mater.*, 2017, **139**, p 39–50. https://doi.org/10.1016/j.actamat.2017.07.056
5. G. Lovicu, E. Paravicini Bagliani, M. De Sanctis, A. Dimatteo, R. Ishak, R. Valentini, Hydrogen Embrittlement of a Medium Carbon Q&P Steel, Metall. Ital. 105 (2013) 3–10
6. X. Zhu, W. Li, H. Zhao, L. Wang, and X. Jin, Hydrogen Trapping Sites and Hydrogen-Induced Cracking in High Strength Quenching & Partitioning (Q&P) Treated Steel, *Int. J. Hydrogen Energy.*, 2014, **39**, p 13031–13040. https://doi.org/10.1016/J.IJHYDENE.2014.06.079
7. A. Drexler, C. Bergmann, G. Manke, V. Kokotin, K. Mraczek, S. Leitner, M. Pohl, and W. Ecker, Local Hydrogen Accumulation After Cold Forming and Heat Treatment in Punched Advanced High Strength Steel Sheets, *J. Alloy. Compd.*, 2021, **856**, p 158226. https://doi.org/10.1016/j.jallcom.2020.158226
8. A. Drexler, C. Bergmann, G. Manke, V. Kokotin, K. Mraczek, M. Pohl, and W. Ecker, On the Local Evaluation of the Hydrogen Susceptibility of Cold-Formed and Heat Treated Advanced High Strength Steel (AHSS) Sheets, *Mater. Sci. Eng. A.*, 2021, **800**, p 140276. https://doi.org/10.1016/j.msea.2020.140276
9. A. Drexler, J. Domitner, C. Sommitsch, Modeling of Hydrogen Diffusion in Slow Strain Rate (SSR) Testing of Notched Samples, 143rd ed., Springer Nature Switzerland AG, 2021. https://doi.org/10.1007/978-3-030-66948-5_6
10. S. Lynch, Discussion of Some Recent Literature on Hydrogen-Embrittlement Mechanisms: Addressing Common Misunderstandings, *Corros. Rev.*, 2019, **37**, p 377–395. https://doi.org/10.1515/corrrev-2019-0017
11. S.P. Lynch, Progress Towards Understanding Mechanisms of Hydrogen Embrittlement and Stress Corrosion Cracking, NACE - Int. Corros. Conf. Ser. 2007 pp 074931–0749355
12. M. Koyama, C.C. Tasan, E. Akiyama, K. Tsuzaki, and D. Raabe, Hydrogen-Assisted Decohesion and Localized Plasticity in Dual-Phase Steel, *Acta Mater.*, 2014, **70**, p 174–187. https://doi.org/10.1016/j.actamat.2014.01.048
13. A. Drexler, B. Helic, Z. Silvayeh, C. Sommitsch, K. Mraczek, and J. Domitner, Influence of Plastic Deformation on the Hydrogen Embrittlement Susceptibility of Dual Phase Steels, *Key. Eng. Mater.*, 2022, **926**, p 2077–2091.
14. D. Eliezer, C.J. Altstetter, The Influence of Austenite Stability on the Hydrogen Embrittlement and Stress-Corrosion Cracking of Stainless Steel, (1979)
15. M. Wasim and M.B. Djukic, Hydrogen Embrittlement of Low Carbon Structural Steel at Macro-, Micro- and Nano-Levels, *Int. J. Hydrogen Energy.*, 2020, **45**, p 2145–2156. https://doi.org/10.1016/j.ijhydene.2019.11.070
16. A. Massone, A. Manhard, A. Drexler, C. Posch, W. Ecker, V. Maier-Kiener, and D. Kiener, Addressing H-Material Interaction in Fast Diffusion Materials—A Feasibility Study on a Complex Phase Steel,

Materials (Basel), 2020, **13**, p 4677. https://doi.org/10.3390/ma13204677

17. A. Massone, A. Manhard, W. Jacob, A. Drexler, W. Ecker, A. Hohenwarter, S. Wurster, and D. Kiener, An SEM Compatible Plasma Cell for In Situ Studies of Hydrogen-Material Interaction, *Rev. Sci. Instrum.*, 2020, **91**, p 043705. https://doi.org/10.1063/1.5142043

18. M. Lin, H. Yu, Y. Ding, G. Wang, V. Olden, A. Alvaro, J. He, and Z. Zhang, A Predictive Model Unifying Hydrogen Enhanced Plasticity and Decohesion, *Scr. Mater.*, 2022, **215**, p 114707. https://doi.org/10.1016/j.scriptamat.2022.114707

19. D. Sasaki, M. Koyama, and H. Noguchi, Factors Affecting Hydrogen-Assisted Cracking in a Commercial Tempered Martensitic steel: Mn Segregation, MnS, and the Stress State Around Abnormal Cracks, *Mater. Sci. Eng. A.*, 2015, **640**, p 72–81. https://doi.org/10.1016/j.msea.2015.05.083

20. M.B. Djukic, V. Sijacki Zeravcic, G.M. Bakic, A. Sedmak, and B. Rajicic, Hydrogen Damage of Steels: A Case Study and Hydrogen Embrittlement Model, *Eng. Fail. Anal.*, 2015, **58**, p 485–498. https://doi.org/10.1016/j.engfailanal.2015.05.017

21. A. Nagao, M. Dadfarnia, B.P. Somerday, P. Sofronis, and R.O. Ritchie, Hydrogen-Enhanced-Plasticity Mediated Decohesion for Hydrogen-Induced Intergranular and "Quasi-Cleavage" Fracture of Lath Martensitic Steels, *J. Mech. Phys. Solids.*, 2018, **112**, p 403–430. https://doi.org/10.1016/j.jmps.2017.12.016

22. M. Wasim, M.B. Djukic, and T.D. Ngo, Corrigendum to "Influence of Hydrogen-Enhanced Plasticity and Decohesion Mechanisms of Hydrogen Embrittlement on the Fracture Resistance of Steel," *Eng. Fail. Anal.*, 2021, **124**, p 105370. https://doi.org/10.1016/j.engfailanal.2021.105370

23. M.B. Djukic, G.M. Bakic, V.S. Zeravcic, A. Sedmak, and B. Rajicic, The Synergistic Action and Interplay of Hydrogen Embrittlement Mechanisms in Steels and Iron: Localized Plasticity and Decohesion, *Eng. Fract. Mech.*, 2019, **216**, p 106528. https://doi.org/10.1016/j.engfracmech.2019.106528

24. C. Meimei Wang, C. Tasan, M. Koyama, D. Ponge, and D. Raabe, Enhancing Hydrogen Embrittlement Resistance of Lath Martensite by Introducing Nano-Films of Interlath Austenite, *Meta. Mater. Trans. A*, 2015, **46**(9), p 3797–3802. https://doi.org/10.1007/s11661-015-3009-y

25. X. Zhu, K. Zhang, W. Li, and X. Jin, Effect of Retained Austenite stability and Morphology on the Hydrogen Embrittlement Susceptibility in Quenching and Partitioning Treated Steels, *Mater. Sci. Eng. A.*, 2016, **658**, p 400–408. https://doi.org/10.1016/J.MSEA.2016.02.026

26. J. Yang, F. Huang, Z. Guo, Y. Rong, and N. Chen, Effect of retained Austenite on the Hydrogen Embrittlement of a Medium Carbon Quenching and Partitioning Steel with Refined Microstructure, *Mater. Sci. Eng. A.*, 2016, **665**, p 76–85. https://doi.org/10.1016/j.msea.2016.04.025

27. L.W. Tsay, M.Y. Chi, Y.F. Wu, J.K. Wu, and D.Y. Lin, Hydrogen Embrittlement Susceptibility and Permeability of Two Ultra-High Strength Steels, *Corros. Sci.*, 2006, **48**, p 1926–1938. https://doi.org/10.1016/j.corsci.2005.05.042

28. G. Pressouyre, A classification of Hydrogen Traps in Steel, *Metall. Trans.*, 1979, **10**(10), p 1571–1573.

29. A. Drexler, T. Depover, S. Leitner, K. Verbeken, and W. Ecker, Microstructural Based Hydrogen Diffusion and Trapping Models Applied to Fe–C X Alloys, *J. Alloys Compd.*, 2020, **826**, p 154057. https://doi.org/10.1016/j.jallcom.2020.154057

30. A. Drexler, T. Depover, K. Verbeken, and W. Ecker, Model-Based Interpretation of Thermal Desorption Spectra of Fe-C-Ti Alloys, *J. Alloys Compd.*, 2019, **789**, p 647–657. https://doi.org/10.1016/j.jallcom.2019.03.102

31. A. Drexler, S. He, R. Pippan, L. Romaner, V.I. Razumovskiy, and W. Ecker, Hydrogen Segregation Near a Crack Tip in Nickel, *Scr. Mater.*, 2021, **194**, p 113697. https://doi.org/10.1016/j.scriptamat.2020.113697

32. A. Drexler, B. Helic, Z. Silvayeh, K. Mraczek, C. Sommitsch, and J. Domitner, The Role of Hydrogen Diffusion, Trapping and Desorption in Dual Phase Steels, *J. Mater. Sci.*, 2022, **57**, p 4789–4805. https://doi.org/10.1007/s10853-021-06830-0

33. A. Drexler, W. Siegl, W. Ecker, M. Tkadletz, G. Klösch, H. Schnideritsch, G. Mori, J. Svoboda, and F.D. Fischer, Cycled Hydrogen Permeation Through Armco Iron – A Joint Experimental and Modeling Approach, *Corros. Sci.*, 2020, **176**, p 109017. https://doi.org/10.1016/j.corsci.2020.109017

34. A. Drexler, L. Vandewalle, T. Depover, K. Verbeken, and J. Domitner, Critical Verification of the Kissinger Theory to Evaluate Thermal Desorption Spectra, *Int. J. Hydrogen Energy.*, 2021, **46**, p 39590–39606. https://doi.org/10.1016/j.ijhydene.2021.09.171

35. A. Drexler, S. He, V. Razumovskiy, L. Romaner, W. Ecker, and R. Pippan, Verification of the Generalised Chemical Potential for Stress-Driven Hydrogen Diffusion in Nickel, *Philos. Mag. Lett.*, 2020, **100**, p 513–523. https://doi.org/10.1080/09500839.2020.1808253

36. Park, Y.D., Maroef, I.S., Landau, A. (2002), Retained Austenite as a Hydrogen Trap in Steel Welds, Weld. Res. 2002, pp 27–35

37. J.H. Ryu, Y.S. Chun, C.S. Lee, H.K.D.H. Bhadeshia, and D.W. Suh, Effect of Deformation on Hydrogen Trapping and Effusion in TRIP-Assisted Steel, *Acta Mater.*, 2012, **60**, p 4085–4092. https://doi.org/10.1016/j.actamat.2012.04.010

38. C.B. Finfrock, D. Bhattacharya, B.N.L. McBride, T.J. Ballard, A.J. Clarke, and D. Clakre, Kester, Decoupling the Impacts of Strain Rate and Temperature on TRIP in a Q&P Steel, *Jom.*, 2022 https://doi.org/10.1007/s11837-021-05039-5

39. C.B. Finfrock, M.M. Thrun, D. Bhattacharya, T.J. Ballard, A.J. Clarke, and K.D. Clarke, Strain Rate Dependent Ductility and Strain Hardening in Q&P Steels, Metall, *Mater. Trans. A Phys. Metall. Mater. Sci.*, 2021, **52**, p 928–942. https://doi.org/10.1007/s11661-020-06127-y

40. X. Wu, H. Lin, Y. Wang, and H. Jiang, Hydrogen Embrittlement and Fracture Mechanism of Friction Stir Welded Quenching and Partitioning 980 Steel, *Mater. Sci. Eng. A.*, 2021, **802**, p 140683. https://doi.org/10.1016/J.MSEA.2020.140683

41. E. Hoyt, E. De Moor, and K.O. Findley, Hydrogen Embrittlement Resistance of High Strength Bar Steel Heat Treated by Quenching and Partitioning, *HT2021 ASM Int.*, 2021, **84147**, p 162–168.

42. Y. Du, X. Gao, L. Lan, X. Qi, H. Wu, L. Du, and R.D.K. Misra, Hydrogen Embrittlement Behavior of High Strength Low Carbon Medium Manganese Steel under Different Heat Treatments, *Int. J. Hydrogen Energy.*, 2019, **44**, p 32292–32306. https://doi.org/10.1016/j.ijhydene.2019.10.103

43. W.T. Geng, A.J. Freeman, R. Wu, C.B. Geller, and J.E. Raynolds, Embrittling and Strengthening Effects of Hydrogen, Boron, and Phosphorus on a Nickel Grain Boundary, *Phys. Rev. B.*, 1999, **60**, p 7149–7155. https://doi.org/10.1103/PhysRevB.60.7149

44. Q. Liu, Q. Zhou, J. Venezuela, M. Zhang, and A. Atrens, Hydrogen Influence on Some Advanced High-Strength Steels, *Corros. Sci.*, 2017, **125**, p 114–138. https://doi.org/10.1016/j.corsci.2017.06.012

45. A. Drexler, W. Ecker, N. Winzer, K. Mraczek, V. Kokotin, G. Manke, C. Bergmann, A step Towards Numerical Evaluation of the Local Hydrogen Susceptibility of Punched and Cold-Formed Advanced High Strength Steel (AHSS) Sheets, In: L. Duprez (Ed.), SteelyHydrogen, Ocas, 2018, p. A02. http://steelyhydrogen2018proc.be/articles/pdf/2

46. J.G. Speer, F.C. RizzoAssunção, D.K. Matlock, and D.V. Edmonds, The "Quenching and Partitioning" Process: Background and Recent Progress, *Mater. Res.*, 2005, **8**, p 417–423. https://doi.org/10.1590/S1516-14392005000400010

47. L. Wang and J.G. Speer, Quenching and Partitioning Steel Heat Treatment, *Metallogr. Microstruct. Anal.*, 2013, **2**, p 268–281. https://doi.org/10.1007/s13632-013-0082-8

48. S. Reisinger, G. Ressel, S. Eck, and S. Marsoner, Differentiation of Grain Orientation with Corrosive and Colour Etching on a Granular Bainitic Steel, *Micron*, 2017, **99**, p 67–73. https://doi.org/10.1016/j.micron.2017.04.002

49. D.L. Bish and S.A. Howard, Quantitative Phase Analysis Using the RIETVELD METHOD, *J. Appl. Crystallogr.*, 1988, **21**, p 86–91. https://doi.org/10.1107/S0021889887009415

50. D. Pérez Escobar, C. Miñambres, L. Duprez, K. Verbeken, and M. Verhaege, Internal and Surface Damage of Multiphase Steels and Pure Iron After Electrochemical Hydrogen Charging, *Corros. Sci.*, 2011, **53**, p 3166–3176. https://doi.org/10.1016/j.corsci.2011.05.060

51. S.V. Brahimi, S. Yue, and K.R. Sriraman, Alloy and Composition Dependence of Hydrogen Embrittlement Susceptibility in High-Strength Steel Fasteners, *Philos. Trans. R. Soc. A Math. Phys. Eng. Sci.*, 2017, **375**(2098), p 20160407. https://doi.org/10.1098/rsta.2016.0407

52. T. Das, S.K. Rajagopalan, S.V. Brahimi, X. Wang, and S. Yue, A Study on the Susceptibility of High Strength Tempered Martensite Steels to Hydrogen Embrittlement (HE) Based on Incremental Step Load (ISL) Testing Methodology, *Mater. Sci. Eng. A.*, 2018, **716**, p 189–207. https://doi.org/10.1016/j.msea.2018.01.032

53. B. Arroyo, L. Andrea, F. Gutiérrez-Solana, and J.A. Álvarez, Time Optimization of the Step Loading Technique in Hydrogen Embrittlement Small Punch Tests, *Theor. Appl. Fract. Mech.*, 2022, **117**, p 103206. https://doi.org/10.1016/j.tafmec.2021.103206

54. American Society for Testing and Materials, ASTM F1624–06 Standard Test Method for Measurement of Hydrogen Embrittlement Threshold in Steel by the Incremental Step Loading Technique, *ASTM B. Stand.*, 2015 https://doi.org/10.1520/F1624-12.2

55. S. Kaar, D. Krizan, R. Schneider, and C. Sommitsch, Impact of Si and Al on Microstructural Evolution and Mechanical Properties of Lean Medium Manganese Quenching and Partitioning Steels, *Steel Res. Int.*, 2020 https://doi.org/10.1002/srin.202000181

56. Y.D. Park, I.S. Maroef, A. Landau, D.L. Olson, Retained Austenite as a Hydrogen Trap in Steel Welds, Weld. J. (Miami, Fla). 2002, 81

57. A. Turner, Steels: Microstructure and Properties, *J. Mech. Work. Technol.*, 1982, **6**, p 389–390. https://doi.org/10.1016/0378-3804(82)90037-7

58. S. Kaar, K. Steineder, R. Schneider, D. Krizan, and C. Sommitsch, New Ms-Formula for Exact Microstructural Prediction of Modern 3rd Generation AHSS Chemistries, *Scr. Mater.*, 2021, **200**, p 113923. https://doi.org/10.1016/j.scriptamat.2021.113923

59. S. Kaar, D. Krizan, R. Schneider, C. Béal, and C. Sommitsch, Effect of Manganese on the Structure-Properties Relationship of Cold Rolled AHSS Treated by a Quenching and Partitioning Process, *Metals*, 2019, **9**(10), p 1122. https://doi.org/10.3390/met9101122

60. E. De Moor, S. Lacroix, A.J. Clarke, J. Penning, and J.G. Speer, Effect of Retained Austenite Stabilized via Quench and Partitioning on the Strain Hardening of Martensitic Steels, *Metall. Mater. Trans. A.*, 2008, **39**, p 2586–2595. https://doi.org/10.1007/s11661-008-9609-z

61. Y.C. Lin, I.E. McCarroll, Y.T. Lin, W.C. Chung, J.M. Cairney, and H.W. Yen, Hydrogen Trapping and Desorption of Dual Precipitates in Tempered Low-Carbon Martensitic Steel, *Acta Mater.*, 2020, **196**, p 516–527. https://doi.org/10.1016/j.actamat.2020.06.046

62. F. Hitzigrath, Bestimmung von diffusiblem Wasserstoff in hochfesten Stählen in Bezug auf die Gitterstruktur, Universität Duisburg- Essen, 2017

63. A. Kuduzović, M. Poletti, C. Sommitsch, M. Domankova, S. Mitsche, and R. Kienreich, Investigations into the Delayed Fracture Susceptibility of 34CrNiMo6 Steel, and the Opportunities for its Application in Ultra-High-Strength Bolts and Fasteners, *Mater. Sci. Eng. A.*, 2014, **590**, p 66–73. https://doi.org/10.1016/j.msea.2013.10.019

64. C.D. Beachem, A New Model for Hydrogen-Assisted Cracking (Hydrogen ''Embrittlement''), *Metall. Mater. Trans. B.*, 1972, **3**, p 441–455. https://doi.org/10.1007/BF02642048

65. M. Nagumo, *Fundamentals of Hydrogen Embrittlement*, Springer Singapore, Singapore, 2016. https://doi.org/10.1007/978-981-10-0161-1

66. J. Rehrl, K. Mraczek, A. Pichler, and E. Werner, Mechanical Properties and Fracture Behavior of Hydrogen Charged Ahss/Uhss Grades at High- and Low Strain Rate Tests, *Mater. Sci. Eng. A.*, 2014, **590**, p 360–367. https://doi.org/10.1016/j.msea.2013.10.044

67. G. Lovicu, M. Bottazzi, F. D'aiuto, M. De Sanctis, A. Dimatteo, C. Santus, and R. Valentini, Hydrogen Embrittlement of Automotive Advanced High-Strength Steels, METALL, *Mater. Trans. A Phys. Metall. Mater. Sci.*, 2012, **43**, p 4075–4087. https://doi.org/10.1007/s11661-012-1280-8

Publisher's Note Springer Nature remains neutral with regard to jurisdictional claims in published maps and institutional affiliations.